HHS Public Access

Author manuscript

Structure. Author manuscript; available in PMC 2024 February 02.

Molecular role of NAA38 in thermostability and catalytic activity of the human NatC N-terminal acetyltransferase

Sunbin Deng[1,2], **Sarah M. Gardner**[3], **Leah Gottlieb**[2], **Buyan Pan**[1], **E James Petersson**[1,4], **Ronen Marmorstein**[1,2,4,*]

[1]Department of Chemistry, 231 South 34th Street, University of Pennsylvania, Philadelphia, PA 19104, USA

[2]Abramson Family Cancer Research Institute, Perelman School of Medicine, University of Pennsylvania, Philadelphia, PA 19104, USA

[3]Graduate Group in Biochemistry and Molecular Biophysics, Perelman School of Medicine, University of Pennsylvania, 421 Curie Boulevard, Philadelphia, PA 19104, USA

[4]Department of Biochemistry and Biophysics, Perelman School of Medicine, University of Pennsylvania, 421 Curie Boulevard, Philadelphia, PA 19104, USA

Summary

N-terminal acetylation occurs on over 80% of human proteins and is catalyzed by a family of N-terminal acetyltransferases (NATs). All NATs contain a small catalytic subunit, while some also contain a large auxiliary subunit that facilitates catalysis and ribosome targeting for co-translational acetylation. NatC is one of the major NATs containing a NAA30 catalytic subunit, but uniquely contains two auxiliary subunits, large NAA35 and small NAA38. Here, we report the cryo-EM structures of human NatC (hNatC) complexes with and without NAA38, together with biochemical studies, to reveal that NAA38 increases the thermostability and broadens the substrate-specificity profile of NatC by ordering an N-terminal segment of NAA35 and reorienting an NAA30 N-terminal peptide binding loop for optimal catalysis, respectively. We also note important differences in engagement with a stabilizing inositol hexaphosphate molecule between human and yeast NatC. These studies provide new insights for the function and evolution of the NatC complex.

Graphical Abstract

*Lead contact and to whom correspondence should be addressed: Ronen Marmorstein, Department of Biochemistry & Biophysics, Abramson Family Cancer Research Institute, Perelman School of Medicine at the University of Pennsylvania, 421 Curie Blvd., Philadelphia, PA 19104, USA, Tel.: (215) 898-7740; Fax: (215) 746-5511; marmor@upenn.edu.

Author Contribution

Conceptualization, S.D., S.G., L.G., B.P., E.J.P. and R.M.; Methodology, S.D., S.G., L.G., B.P., E.J.P. and R.M.; Investigation, S.D., S.G. B.P., and L.G.; Formal Analysis, S.D; Writing – Original Draft, S.D.; Visualization, S.D.; Writing – Review and Editing, S.D., S.G, L.G., B.P., E.J.P. and R.M.; Funding Acquisition, R.M. and E.J.P.; Resources, R.M.; Supervision, R.M. and E.J.P.

Declaration of interests

The authors declare no competing interests.

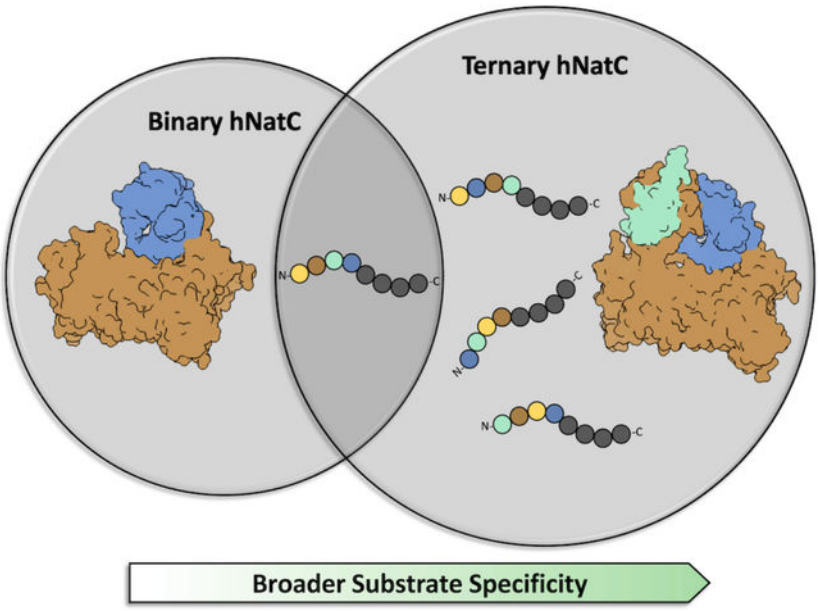

eTOC Blurb

The N-terminal acetyltransferases NatC uniquely requires a third small Naa38 subunit for activity. Deng et al. finds that Naa38 increases the thermostability and broadens the substrate-specificity profile of NatC by ordering an N-terminal segment of NAA35 and reorienting an NAA30 N-terminal peptide binding loop for optimal catalysis, respectively.

Introduction

N-terminal acetylation (NTA) is one of the most common protein modifications, which occurs predominantly in a co-translational manner[1,2]. This modification can affect protein stability, function, localization, degradation, interaction, and complex formation[3–8]. N-terminal acetyltransferases (NATs) mediate NTA by transfering the acetyl group from the donor acetyl-CoA to the α-amino group of the first amino acid residue of their specific protein substrates[9]. While these enzymes are single subunit proteins in bacteria and archaea, some eukaryotic NATs have evolved to function as multi-subunit protein complexes, which harbor auxiliary subunits, associate with regulatory proteins and small molecules, and interact with the ribosome to mediate co-translational acetylation[9]. The increased complexity of N-terminal acetylation in eukaryotes likely relates to the greater abundance of this modification in eukaryotes (~70%) and its coordination with other activities compared to bacterial and archaea (~20%)[3].

In humans, there are minimally seven NATs, NatA-NatF and NatH. Among them, NatC is one of the major NATs, along with NatA, NatE, and NatB, covering most of the human Nt-acetylome[3]. NatC is a heterotrimeric protein complex, consisting of a catalytic subunit, NAA30, and two auxiliary subunits – the large (725 residues) NAA35 subunit and the small (125 residues) NAA38 subunit. While all other multimeric NATs contain a single eukaryotic-conserved auxiliary subunit, NatC is the only NAT to contain

an additional small auxiliary subunit that is conserved in eukaryotes. NatC has been suggested to use its large auxiliary subunit[10] in order to associate with the ribosome for co-translational acetylation[2] and is reported to primarily acetylate N-terminal methionine of nascent substrates starting with Met-Leu-, Met-Phe-, Met-Ile, Met-Tyr-, Met-Lys-, and Met-Trp-[11,12], a sequence profile that overlaps with NatE[13,14]. Deletion of the NatC subunits in the yeast *Saccharomyces cerevisiae* (*Sc*NatC) results in similar growth growth phenotype abnormalities including diminished growth on media containing nonfermentable carbon sources[11], while deletion of human NatC (hNatC) in cell culture leads to reduced viability, p53-dependent apoptosis, and a reduction in both mitochondrial and Golgi integrity[12,15,16].

Our recently reported cryo-EM structure of the ternary *S. pombe* NatC (*Sp*NatC)[17], together with the reported crystal structures of *S. cerevisiae* NatC (*Sc*NatC)[10], has revealed the unique architecture of NatC compared to other NATs and has provided important insights into its mechanism of substrate-specific recognition and catalysis. Although the molecular role of NAA38 could be inferred through the ternary structures, the absence of a binary NAA30/NAA35 structure limits the ability to directly validate the role of NAA38. In addition, the absence of a biochemical and structural analysis of the human NatC has restricted insight into potentially unique features of the human complex. In this study, we prepared binary hNAA30/hNAA35 and ternary hNAA30/hNAA35/hNAA38 complexes for biochemical studies and cryo-EM structure determination with a NatC/E peptide substrate. Our studies reveal the molecular basis for how NAA38 promotes NatC complex thermostability and broadens the substrate-specificity profile of NatC, and highlights important differences between human and yeast NatC complexes in engagement with a stabilizing inositol hexaphosphate (IP_6) molecule. These studies provide new insights into the function and evolution of NatC.

Results

Contributions of NAA38 to hNatC substrate profile and thermostability

During initial recombinant protein overexpression studies, we discovered that we could co-express and purify a “binary hNatC” subcomplex containing an N-terminally truncated NAA35 (truncating residues 1–27 of 725 residues) and N-terminally truncated NAA30 (truncating residues 1–210 of 362 residues) from baculovirus-infected Sf9 cells (Figure 1A). We were also able to reconstitute the holo “heterotrimeric hNatC” complex through co-purification of the binary hNatC subcomplex with full length hNAA38 that had been overexpressed in *E. coli*. To evaluate the activity of these complexes towards NatC-only, NatC/E and NatE-only cognate-substrates, we assayed the NatC complexes against peptides containing the following sequences: MLRF (a NatC only substrate); MKLN, MLGP and MFPA (NatC/E substrates); and MADD (a NatE substrate)(Full peptide sequences can be found in Materials and Methods) (Figure 1B). Surprisingly, we found that while the binary complex was strongly selective for the NatC-only MLRF substrate over the NatC/E substrates, the ternary complex showed comparable activity towards all NatC and NatC/E peptide substrates (Figure 1B). Additionally, the binary and ternary complexes only displayed significant differences in activity towards the NatC/E peptide substrates (Figure

1C). Thus, hNatC can exist in both binary and ternary states, and NAA38 appears to shift hNatC to more effectively modify non-optimal NatC substrates.

To evaluate the thermostability of the binary and ternary hNatC complexes, we performed differential scanning fluorimetry (DSF). While ternary hNatC showed a melting temperature of 51.6 ± 0.2 °C, the binary hNatC displayed a melting temperature about 2 degrees lower at 49.5 ± 0.1 °C (Figure 1D), thus demonstrating that NAA38 also contributes to hNatC thermostability.

We previously demonstrated that both yeast[18] and human[19,20] NatE and NatA can bind to the small molecule inositol hexaphosphate (IP_6), and that this binding increases the thermostability of its receptor proteins. Structures of these proteins with IP_6 have also revealed that the small molecule binds to unique binding pockets at the interface of the catalytic and auxiliary subunits[18–20]. Recently, we also reported that IP_6 significantly increases yeast NatC thermostability, as observed by DSF, and that IP_6 binds to *Sp*NatC at the interface of *Sp*Naa30 and *Sp*Naa35, particularly in close proximity to the peptide substrate binding site[17]. These results led us to hypothesize that IP_6 might similarly increase hNatC stability. Surprisingly, when IP_6 was incorporated into the DSF experiment, we did not observe a significant change in melting temperature of either the binary or ternary hNatC complexes (Figure 1D). As a negative control, hNatB, a NAT complex that has not been found to bind IP_6[21], also had almost identical melting temperatures in the presence and absence of IP_6 (Figure 1D). These results suggest that the hNatC complexes have diverged from their yeast orthologs, losing the requirement of IP_6 binding for complex thermostability.

Overall architecture of hNatC

We determined the single particle cryo-EM structures of both the ternary and binary hNatC complexes prepared in the presence of IP_6 and CoA-MLGP, a bisubstrate analogue containing an NatC/E sequence, to overall map resolutions of 3.64 and 3.09 Å, respectively (Supplementary Figure 2 and Supplementary Figure 3). The EM map of ternary hNatC was reconstituted using 172,041 particles selected from 5,372 raw electron micrographs and binary hNatC was reconstituted using 192,437 particles from 4,222 raw electron micrographs. The ternary model was built using *Sp*NatC (PDB: 7L1K) and the binary model was built using the same ternary structure but with hNAA38 excluded from the starting model. In the ternary hNatC model, the N-terminal residues 1–35 and C-terminal residues 116–125 of hNAA38 could not be traced into the map and, therefore, are presumed to be disordered. In the binary hNatC model, the N-terminal hNAA35 residues, 28–83, could not be traced into the map and are also presumed to be disordered. The details for the model refinement statistics are summarized in Table 1, while the model and map fit-in quality is highlighted in Supplementary Figure 4. Consistent with our biochemical data, we were unable to find density corresponding to IP_6 in either structure, despite the addition of the small molecule during cryo-EM sample preparation.

Although the human and yeast NatC proteins only have 33% - 35% sequence identity, we found that the overall ternary hNatC architecture is very similar to both species of yeast NatC complexes (Figure 2). Like in the yeast structures, hNAA35 serves as the

central docking hub for both hNAA30 and hNAA38[10,17]. hNAA38 interacts slightly with hNAA30-α2 but closely with the hNAA35 N-terminal portion. Ternary hNatC aligns well to both *Sp*NatC (PDB: 7L1K) and *Sc*NatC (PDB: 6YGB) – with a root-mean-square deviation (RMSD) values of 2.809 Å (over 624 common Cα atoms) and 3.541 Å (over 519 common Cα atoms), respectively. Based on this alignment comparison, it appears that hNatC is structurally more closely related to *Sp*NatC than *Sc*NatC. The most significant structural differences between *Sc*NatC and the hNatC/*Sp*NatC map to the *Sc*NAA35 subunit. In particular, *Sc*NAA35 contains two additional short helices that flank the outside surface of NAA38 and an unusually long α-helix that juts out of the NAA35 core and loops back to an additional helix that brings the chain back to the core (Figure 2, **right**). In the *Sc*NatC structure, residues at the C-terminal end of the long helix and N-terminal end of the following helix (referred to as electro-positive region 2, ERP2[10]) were shown to be involved in ribosome binding, thus suggesting potential differences in how *Sc*NatC and hNatC bind to ribosomes.

Molecular basis for the impact of hNAA38 on hNatC complex stability and catalytic activity

To directly evaluate the molecular role of hNAA38 in hNatC stability and catalytic activity towards a NatC/E substrate, we overlaid the binary and ternary structures for comparison. Overall, the binary and ternary hNatC complexes superimpose well, with an RMSD of 0.598 Å (over 670 common ordered Cα atoms). However, upon close inspection, there are notable local hNAA38-induced structural rearrangements. Strikingly, N-terminal hNAA35 residues 28–83 are disordered in the binary complex but are ordered in the ternary complex (Figure 3A, Supplementary Figure 4A). In the ternary complex, these hNAA35 residues wrap around hNAA38 through two short α-helices, three short β-strands, and a series of loops. In addition, hNAA35 residues 305–319 shift towards the core of the hNAA35 in the ternary complex to avoid a clash with the hNAA38 loop residues 69–74 (Figures 3B and 3C, Supplementary Figure 4A). Together, the overall reduced secondary structure content of the binary complex correlates with its reduced thermostability relative to the ternary complex correlates.

The absence of hNAA38 has a negative impact directly on the N-terminal peptide binding site configuration in the hNAA30 active site. In the ternary complex, we were able to model the first four residues of the N-terminal peptide region of the bisubstrate inhibitor, while in the binary complex we were only able to model the first two residues. This key discrepancy between the two complexes suggests that hNAA38 plays an important role in substrate recognition, where hNAA38 enhances hNatC binding to the third and fourth substrate residues (Figure 4A). Similar to previous observations in the ternary yeast NatC complexes[10,17], N-terminal peptide binding in the ternary hNatC complex is largely mediated by residues in the α1-α2 and β6-β7 loops. Specifically, within the α1-α2 loop, L235 makes van der Waals contacts with peptide region Met1 while E237 and Y239 form hydrogen bonds to the peptide backbone carbonyl and amino group of Leu2, respectively (Figure 4B). However, in the binary complex, these key residues in the α1-α2 loop is located further away from the peptide binding site, resulting in suboptimal peptide contacts (Figure 4B). In particular, without hNAA38, E237 flips ~180° away from the peptide binding site (Figure 4B). Within the β6-β7 loop, both Y347 and Y348 make van der Waals

and backbone carbonyl interactions with the peptide Gly3, while Y348 also hydrogen bonds with the peptide Met1 backbone carbonyl (Figure 4C). Similar to the α1-α2 loop, Y347 and Y348 within the β6-β7 loop move further away from the peptide binding region in the absence of hNAA38 (Figure 4C). Notably, the previously described key catalytic residues of yeast NatC[10,17] - E321 and Y333 in the human ortholog - maintain similar positions in both the binary and ternary human complexes (Figure 4D). Residues responsible for contact with acetyl-CoA are also largely maintained between the binary and ternary human complexes (Supplemental Figure 5). hNAA38 therefore appears to play a key role played in hNatC catalysis by properly positioning important N-terminal peptide binding residues within the hNAA30 α1-α2 loop.

The observation that key catalytic residues, E321 and Y33, maintain the same position in the binary and ternary complexes implies that both the binary and ternary complexes would be active towards some of the substrates, consistent with the ability of both complexes to process the MLRF NatC substrate (Figure 1B). Our observation that the ternary, but not the binary complex, can process the MLGP NatC/E substrate suggests a broader substrate profile for the ternary complex. This likely arises from the additional interactions mediated by Y347 and Y348 within the β6-β7 loop, which move closer to residue 3 for more stable interactions in the ternary complex.

Molecular basis for the suboptimal IP_6 binding properties of hNatC

Since the binary and ternary hNatC complexes are structured similarly around the putative IP_6 binding region, we used the ternary hNatC structure to rationalize the loss of IP_6 engagement by hNatC we previously observed. An overlay of the ternary hNatC structure with the IP_6-bound *Sp*NatC structure (PDB: 7L1K) with the ternary hNatC structure, reveals that the IP_6 binding site is largely maintained in hNatC, which is consistent with the observation that the residues reported to be responsible for IP_6 binding are mostly conserved from yeast to human[17]. In fact, most of these residues in hNatC are positioned to potentially enable IP_6 engagement, including residues His275, Lys276, Arg281, Lys341, and Arg356 from hNAA30, and residues Arg445 and His452 from hNAA35 (Figure 5). However, it is noteworthy that residues – one in hNaa30 and one in hNAA35 – located within the putative IP_6 binding site are not conserved: an Arg residue in *Sp*NatC is replaced with the acidic Asp448 residue in hNAA35; and a Tyr residue in *Sp*NatC is replaced with the acidic Asp341 residue in hNAA30 (Figure 5). The positions of both hNAA30 Asp341 and Asp448 side chains would disfavor IP_6 binding, with Asp341 located too far away to make a productive interaction with IP_6 and the flanking basic residues and Asp448 mediating charged-charged repulsion with the negatively charged phosphate groups in the IP_6 molecule. In addition, the conserved hNAA30-Arg281, which interacts with IP_6 in *Sp*NatC, is disordered in the human structure, likely because of the absence of bound IP_6 (Figure 5). Taken together, hNatC appears to contain a suboptimal binding site for IP_6 and has, thus, likely diverged in its requirement for IP_6 binding for stability.

Discussion

NatC is a major and unique member of the NAT protein family in that it harbors two auxiliary subunits, the large NAA35 and the small NAA38, that has been shown to play an important functional role in maintaining mitochondrial and Golgi integrity[12,22]. In this study, we produced recombinant hNatC complexes with and without hNAA38, and carried out biochemical and structural characterization of these complexes to reveal two important activities of NAA38: To increase hNatC thermostability through the ordering of an N-terminal hNAA30 region and to broaden the substrate-specificity profile of hNatC by reorienting the α1-α2 and β6-β7 substrate binding loops. Key catalytic residues maintain their positions in both the binary and ternary complexes, which is consistent with our data that the binary complex is able to process some NatC substrates. We also found that, unlike the yeast NatC complexes, hNatC is not stabilized by an IP_6 molecule due to a suboptimal IP_6 binding site.

While superposition of the evolutionarily conserved catalytic domain of hNAA30 shows high structural conservation between yeast and human hNAA30, the human protein contains a unique N-terminal region of ~200 residues (Supplementary Figrue 1A). While this region was not included in the current analysis, an AlphaFold structural prediction[23] suggests that this region is largely unstructured, except for the low confidence prediction of two helices predicted to be positioned on the surface of hNAA30 opposite to the hNAA35 auxiliary subunit. The functional role of this N-terminal region is unclear, but given the absence of the *Sc*NatC ribosome interaction region, TPR2, in hNatC, the human enzyme might compensate by using its unique N-terminal region for ribosome binding. The N-terminal region of hNAA30 has also been shown to harbor sites of phosphorylation, pointing to another potential functional role[24].

The NAA38 subunits of the NatC complex is a member of the Sm-like (LSm) family of small proteins that are involved in several different aspects of RNA processing and regulation including RNA binding and are highly conserved in eukaryotes[25]. Proteins in this family contain a conserved Sm fold that comprises a β-barrel structure packed against an α-helix and often multimerize to form ring-like structures[26]. As NAT auxiliary subunits are often helix-rich[9], it is unusual that NatC contains an evolutionarily conserved β-rich auxiliary subunit that is typically involved in RNA metabolism. While the reason for this remains unclear, it is possible that NAA38 may play an additional important role in facilitating NatC association with the ribosome as a result of the ability of NAA38 to bind to RNA. Interestingly, there is a precedent for NAT-RNA engagement, which was observed in the structure of a yeast NatE/ribosome complex where it was revealed that the rRNA expansion segments of the ribosome play a particularly important role in NatE association[27]. As LSm proteins can also harbor RNA binding specificity, RNA interactions mediated by NAA38 could be involved in promoting ribosome binding specificity.

The current literature suggests that NAA38 is an obligate subunit for native NatC function[11], suggesting that a binary NatC complex without NAA38, and with more selective substrate specificity as shown in this study, may not exist in cells. This argues that the endogenous activity of the heterotrimeric NatC, with bound NAA38, would exhibit a broader substrate

specificity, that overlaps with NatE specificity as observed in this study with the ternary hNatC complex.

Given the importance and unique contribution of NAA38 to NatC function, the development of small molecule compounds that inhibit binding of NAA38 to NatC could provide useful tools to further probe the specific contribution of the NatC member of the NAT family of proteins to human biology. Such an inhibitor could be instrumental in probing the specific role of hNatC in cancer, as NATs are often dysregulated in many tumors[28]. Together, the described studies reinforce the conserved role of NAA38 in optimal NatC function.

STAR Methods

RESOURCE AVAILABILITY

Lead Contact—Further information and requests for resources and reagents should be directed to and will be fulfilled by the Lead Contact, Ronen Marmorstein (marmor@upenn.edu).

Materials Availability—Primary data and plasmids generated in this study are available upon request from the corresponding author.

Data and Code availability

- The cryo-electron microscopy maps and atomic coordinates for both the ternary and binary hNatC have been deposited onto the EMDataBank (accession codes EMD-24070 and EMD-24393, respectively) and the ProteinDataBank (PDB accession codes: 7MX2 and 7RB3, respectively). Primary data are available upon reasonable request from the corresponding author.
- This paper does not report original code.
- Any additional information required to reanalyze the data reported in this paper is available from the lead contact upon request.

EXPERIMENTAL MODEL AND SUBJECT DETAILS

We used Spodoptera frugiperda (Sf9) cells cultured in SFM II medium for the recombinant expression of binary and ternary hNatC complexes for biochemical experiments and cryo-EM structural studies. We used *E. coli* cells to prepare recombinant hNAA38 for reconstituion with binary hNatC to prepare recombinant ternary NatC for biochemical experiments and cryo-EM structural studies. See Methods Details.

METHODS DETAILS

Binary hNatC Expression and Purification.—Recombinant hNAA30 and hNAA35 proteins were prepared that contained the evolutionarily conserved catalytic and auxiliary domains, resulting in the deletions or residues 1–210 and 1–27 of hNAA30 and hNAA35, respectively (hNAA30$^{211-362}$ and hNAA35$^{28-725}$) (Supplementary Figures 1A and 1B). DNA constructs were cloned into a modified pFastBac DUAL vector containing an N-terminal poly-histidine tag and a tobacco etch virus (TEV) cleavage site on hNAA35.

Recombinant binary hNatC protein was produced using an Sf9 expression system (ThermoFisher, cat #12659017) and purified at 4°C. Protein expresison was achieved using high density (2×10^6 cells * mL^{-1}) suspension cultures of Sf9 cells that were infected at a multiplicity of infection of ~1 in Fernbach Shake flasks at 27 °C. Cells were harvested by centrifugation 48 hours post infection and resuspended in lysis buffer (25 mM Tris pH 8.0, 300 mM NaCl, 10 mM Imidazole, 10 mM β-mercaptoethanol (β-ME) that was supplemented with DNase and a complete EDTA-free Protease inhibitor cocktail (Roche). After cell lysis by sonication, and lysate clarification by centrifugation, the clarified supernatant was passed over Ni-NTA resin (Thermo Scientific), which was subsequently washed with ~10 column volumes (CVs) of lysis buffer. The protein was batch eluted in a buffer containing 25 mM Tris pH 8.0, 200 mM NaCl, 200 mM Imidazole, 10 mM β-ME. The eluate was dialyzed overnight into a buffer containing 25 mM HEPES, pH 7.5, 200 mM NaCl, 10 mM β-ME with TEV protease added for tag removal. The solution was loaded onto a 5-mL HiTrap SP ion-exchange column (GE Healthcare) for ion-exchange and eluted with a salt gradient (200–1000 mM NaCl) over 10 CVs. Peak fractions were concentrated using a 100 KDa MWCO centrifugal filter (Amicon Ultra, Millipore) and loaded on to a S200prep gel-filtration column (GE Healthcare) in a buffer containing 25 mM HEPES pH 7.0, 200 mM NaCl and 1 mM TCEP (tris(2-carboxyethyl)phosphine) (Gold Biotechnology). Purified proteins was snap-frozen in the liquid nitrogen and stored in −80°C for later use.

Ternary hNatC Expression and Purification—Full-length $hNAA38^{1-125}$ was cloned into a pRSF vector with an N-terminal GST tag and a TEV cleavage site. The recombinant protein was expressed in Rosetta (DE3)pLysS *E. coli* cells where transformed cells were cultured at 37 °C until the absorbance A_{600} reached ~0.7 and GST-$NAA38^{1-125}$ overexpression was induced using 0.5 mM IPTG (isopropyl 1-thio-β-D-galactopyranoside) (Gold Biotechnology) at 16°C overnight with agitation.

To prepare purified GST-$hNAA38^{1-125}$, cells were resuspended in 25 mM Tris pH 8.0, 300 mM NaCl,10 mM β-ME, and 2 mM PMSF (phenylmethylsulfonyl fluoride) (ThermoFisher) and lysed by probe sonication and clarified by centrifugation. All subsequent steps were conducted at 4°C. The clarified supernatant was incubated with glutathione agarose resin (ThermoFisher) for ~1 hour. The resin was subsequently washed with 10 CVs of lysis buffer and the protein was eluted with lysis buffer containing 10 mM reduced glutathione (ThermoFisher). The eluate was concentrated and further purified to homogeneity using a Superdex 75 gel filtration column (GE Healthcare) in storage buffer containing 25 mM HEPES, pH 7.0, 200 mM NaCl, and 1 mM TCEP.

To obtain the ternary NatC complex, 3 L of Sf9 cells expressing binary hNatC (hNAA30 and hNAA35) and 2 L of *E. coli* cells expressing hNAA38 were co-lysed in the lysis buffer using sonication and purified using the same method as described above for binary hNatC.

Acetyltransferase Activity Assay—Assays were carried out at room temperature in a reaction buffer containing 75 mM HEPES, pH 7.0, 120 mM NaCl, 1 mM DTT as described previously[18]. The full sequence of peptide substrates of “MLGP” peptide (NatC/E-type, GenScript) is: NH_2-MLGPEGGRWGRPVGRRRRP-COOH, “MKLN” peptide (NatC/E-type, Genscript) is: NH_2-MKLNISFRWGRPVGRRRRP-COOH, “MFPA” peptide (NatC/

E-type, Genscript) is NH_2-MFPAAPSRWGRPVGRRRRP-COOH, "MADD" peptide (NatE-type, Genscript) is: NH_2-MADDLDFRWGRPVGRRRRP-COOH, and "MLRF (NatC-type, GenScript) is: NH_2-MLRFVTKRWGRPVGRRRRP-COOH). The first seven residues of "MLGP" represent the N-terminus of hnRNP F[29], the first seven residues of "MLKN" peptide represent the N-terminus of the 40S ribosomal protein S6[12], the first seven residues of the "MFPA" peptide represent the N-terminus of the nuclear pore complex protein Nup133[12], the first seven residues of the "MADD" peptide represent the N-termini of eukaryotic translation initation factor 5A[12], and the first seven residues of "MLRF" represent the N-terminus of the major capsid protein (gag) of *S. cerevisiae* virus L-A[30]. The additional seventeen residues of all peptide are derived from the sequence of adrenocorticotropic hormone (ACTH) with all Lys residue substituted to Arg to facilitate peptide capture on the negatively charged P81 paper for quantifying protein acetylation[29]. To compare the activities of binary and ternary NatC activity against the peptide substrates, 50 nM enzyme (or buffer control with MLRF peptide to monitor chemical acetylation) was mixed with 50 μM Ac-CoA (^{14}C-labeled, 4 mCi $mmol^{-1}$; PerkinElmer Life Sciences) and 300 μM peptide, and allowed to react for 2, 4, 6, 8, 10 min before being quenched by blotting onto P81 paper (St. Vincent's Institute Medical Research) for scintillation counting (Packard Tri-Carb 1500 liquid scintillation analyzer) resulting in independent replicates. An acetyl-CoA standard curve was utilized to determine pmol product produced and time courses were fit with linear regression models to get average rate of reaction (pmol/min). Assays were performed as technical duplicates (Binary peptides MLRF, MKLN, MLGP) and triplicates (all others). A one-way ANOVA was used to compare the effect of peptide substrate on activity and a unpaired t-test was utilized to analyze differences in activity between binary and ternary NatC complexes. Analysis was performed in Prism.

Differential Scanning Fluorimetry Assay—Sypro Orange (5000X stock, ThermoFisher Scientific) was diluted 1:500 and 10 μL was mixed with 10 μL solution containing 2 mg mL^{-1} protein with or without 10 μM IP_6 (Source) in buffer containing 25 mM HEPES, pH 7.0, 200 mM NaCl, and 1 mM TCEP. Fluorescent readings were recorded using a qPCR (ABI 7900 RealTime PCR), which was heated from 20 °C to 95 °C using a 2% ramp rate. The raw data was analyzed using DSF world[31]. DSF scans of all samples were performed as a series of three technical replicates. Error bars in the figure indicate the Standard Deviation (SD) of each condition. The negative control, hNatB, used in this assay was prepared as described previously[21].

Cryo-EM Data Collection—For hNatC binary and ternary hNatC complexes, 5 mg mL^{-1} of enzyme was mixed with three molar-excess of both CoA-MLGP bisubstrate inhibitor and IP_6 (1 mM). To improve the random orientation of the protein complex particles, 4 mM CHAPSO (ThermoFisher) was also incorporated. 3 μL of this mixed sample was applied to glow-discharged Quantifoil R1.2/1.3 holey carbon support grids, blotted, and plunged into liquid ethane using an FEI Vitrobot Mark IV. An FEI TF20 was used for screening the grids and data collection was performed with a Titan Krios equipped with a K3 Summit direct detector (Gatan) at a magnification of 105,000 × and defocus values set from −0.1 to −3.0 μm. Each stack was exposed and counted in super-resolution mode with a total dose of 42 e^-

Å^{-2}, resulting in 35 frames per stack. Image stacks were automatically collected with EPU. A full description of the Cryo-EM data collection parameters can be found in Table 1.

Cryo-EM Data Processing—Original image stacks (with pixel size of 0.42 Å pixel^{-1}) were summed and corrected for drift and beam-induced motion at the micrograph level using MotionCor2[32]; and binned twofold, resulting in a pixel size of 0.84 Å pixel^{-1}. After motion correction in Relion 3.1.1[33], defocus estimation and the resolution range determination of each micrograph was performed with CTFFIND-4.1[34].

For ternary NatC reconstruction (Supplementary Figure 2), a total of 5,372 images were collected. In Relion-3.1.1[33], Laplacian-of-Gaussian (with a diameter set between 100 Å and 200 Å) was used to auto-pick 3,618,204 particles. 2D classifications were performed on these particles and representative 2D classes were used as 2D references to template the auto-picking of 1,785,742 particles. After bad particles were removed by two runs of 2D classification, 1,514,531 particles from good classes were used to generate an Ab-Initio model. 3D classification (with 4 classes) was performed, and the good class was selected as a 3D reference to template pick 1,606,636 particles. After 2D and 3D classification were performed to remove bad particles, a selection of a total of 650,653 particle was transferred to cryoSPARC V3.1.0[35] for further data processing. In cryoSPARC[35], 2D classification was further used to remove bad particles, and the remaining 409,177 particles were used to generate four Ab-initio models. Two rounds of heterogeneous refinement were performed to further remove bad particles. 172,041 particles were used for auto-refinement and per particle CTF refinement. The final map was refined to an overall map resolution of 3.64 Å (model resolution of 3.8 Å), with local resolution estimated using cryo-SPARC[35].

For binary NatC reconstruction (Supplementary Figure 3), a total of 4,222 images were collected and a similar workflow was performed. The ternary NatC model was used as reference to autopick 2,539,386 particles. After bad particles were removed by 2D and 3D classification, 375,683 “good” particles from Relion-3.1.1 were transferred to cryoSPARC V3.1.0 for further data processing. In cryoSPARC, bad particles were further removed by 2D classification and heterogeneous refinement so that 192,437 particles were used for auto-refinement and per particle CTF refinement. The final map was refined to an overall map resolution of 3.09 Å (model resolution of 3.4 Å), with local resolution estimated in cryo-SPARC[35].

Cryo-EM Model Building and Refinement—The ternary hNatC atomic model was built manually using the program COOT[36] according to the Cryo-EM map, as guided by the predicted secondary structure[37] (http://bioinf.cs.ucl.ac.uk/psipred/) and bulky residues such as Phe, Tyr, Trp, and Arg. The complete model was then refined using real-space refinement in PHENIX[38]. All representations of Cryo-EM density and structural models were prepared using Chimera[39] and PyMol[40] (https://pymol.org/2/). The binary hNatC atomic model was built using the ternary hNatC structure as the starting model and refined as described above.

Quantification and statistical analysis—In Figure 1b, acetylation activity data shows standard error (SEM), n = 3. One way ANOVA was utilized to calculate P-values.

In Figure 1c, acetylation activity data shows standard error (SEM) errors, n = 3. Unpaired t-test was utilized to calculate P-values.

In Figure 1d, differential scanning fluorimetry (DSF) assay data shows standard deviation (SD) errors, n = 3.

In Supplementary Figure. 1, acetylation activity data shows standard deviation (SD) errors, n = 3.

Supplementary Material

Refer to Web version on PubMed Central for supplementary material.

ACKNOWLEDGEMENTS.

This work was supported by NIH grants R35 GM118090 awarded to R.M and R01 NS103873 awarded to E.J.P. S.G. and L.G. were supported by NIH training grants T32 GM132039 and T32 GM071339, respectively. We thank the University of Pennsylvania Electron Microscopy Resource Lab for initial cryo-grids screening; and Stefan Steimle at the Beckman Center for Cryo-EM at the University of Pennsylvania for technical assistance on data collection. B.P. thanks the University of Pennsylvania for support through a Dissertation Completion Fellowship.

Inclusion and diversity

We support inclusive, diverse, and equitable conduct of research.

Reference

1. Aksnes H, Ree R, and Arnesen T (2019). Co-translational, Post-translational, and Non-catalytic Roles of N-Terminal Acetyltransferases. Mol Cell 73, 1097–1114. [PubMed: 30878283]
2. Polevoda B, Brown S, Cardillo TS, Rigby S, and Sherman F (2008). Yeast N(alpha)-terminal acetyltransferases are associated with ribosomes. J Cell Biochem 103, 492–508. [PubMed: 17541948]
3. Aksnes H, Drazic A, Marie M, and Arnesen T (2016). First Things First: Vital Protein Marks by N-Terminal Acetyltransferases. Trends Biochem Sci 41, 746–760. [PubMed: 27498224]
4. Setty SRG, Strochlic TI, Tong AHY, Boone C, and Burd CG (2004). Golgi targeting of ARF-like GTPase Arl3p requires its Nα-acetylation and the integral membrane protein Sys1p. Nature Cell Biology 6, 414. [PubMed: 15077114]
5. Forte GM, Pool MR, and Stirling CJ (2011). N-terminal acetylation inhibits protein targeting to the endoplasmic reticulum. PLoS Biol 9, e1001073. [PubMed: 21655302]
6. Arnesen T (2011). Towards a functional understanding of protein N-terminal acetylation. PLoS Biol 9, e1001074. [PubMed: 21655309]
7. Hwang CS, Shemorry A, and Varshavsky A (2010). N-terminal acetylation of cellular proteins creates specific degradation signals. Science 327, 973–977. [PubMed: 20110468]
8. Scott DC, Monda JK, Bennett EJ, Harper JW, and Schulman BA (2011). N-terminal acetylation acts as an avidity enhancer within an interconnected multiprotein complex. Science 334, 674–678. [PubMed: 21940857]
9. Deng S, and Marmorstein R (2021). Protein N-Terminal Acetylation: Structural Basis, Mechanism, Versatility, and Regulation. Trends Biochem Sci 46, 15–27. [PubMed: 32912665]
10. Grunwald S, Hopf LVM, Bock-Bierbaum T, Lally CCM, Spahn CMT, and Daumke O (2020). Divergent architecture of the heterotrimeric NatC complex explains N-terminal acetylation of cognate substrates. Nature communications 11, 5506.
11. Polevoda B, and Sherman F (2001). NatC Nalpha-terminal acetyltransferase of yeast contains three subunits, Mak3p, Mak10p, and Mak31p. J Biol Chem 276, 20154–20159. [PubMed: 11274203]

12. Van Damme P, Kalvik TV, Starheim KK, Jonckheere V, Myklebust LM, Menschaert G, Varhaug JE, Gevaert K, and Arnesen T (2016). A Role for Human N-alpha Acetyltransferase 30 (Naa30) in Maintaining Mitochondrial Integrity. Mol Cell Proteomics 15, 3361–3372. [PubMed: 27694331]
13. Van Damme P, Hole K, Gevaert K, and Arnesen T (2015). N-terminal acetylome analysis reveals the specificity of Naa50 (Nat5) and suggests a kinetic competition between N-terminal acetyltransferases and methionine aminopeptidases. Proteomics 15, 2436–2446. [PubMed: 25886145]
14. Van Damme P, Evjenth R, Foyn H, Demeyer K, De Bock PJ, Lillehaug JR, Vandekerckhove J, Arnesen T, and Gevaert K (2011). Proteome-derived peptide libraries allow detailed analysis of the substrate specificities of N(alpha)-acetyltransferases and point to hNaa10p as the post-translational actin N(alpha)-acetyltransferase. Mol Cell Proteomics 10, M110 004580.
15. Starheim KK, Gromyko D, Evjenth R, Ryningen A, Varhaug JE, Lillehaug JR, and Arnesen T (2009). Knockdown of human N alpha-terminal acetyltransferase complex C leads to p53-dependent apoptosis and aberrant human Arl8b localization. Mol Cell Biol 29, 3569–3581. [PubMed: 19398576]
16. Starheim Kristian K., Kalvik Thomas V., Bjørkøy G, and Arnesen T (2017). Depletion of the human N-terminal acetyltransferase hNaa30 disrupts Golgi integrity and ARFRP1 localization. Bioscience Reports 37.
17. Deng S, Gottlieb L, Pan B, Supplee J, Wei X, Petersson EJ, and Marmorstein R (2021). Molecular mechanism of N-terminal acetylation by the ternary NatC complex. Structure 29, 1094–1104 e1094. [PubMed: 34019809]
18. Deng S, Magin RS, Wei X, Pan B, Petersson EJ, and Marmorstein R (2019). Structure and Mechanism of Acetylation by the N-Terminal Dual Enzyme NatA/Naa50 Complex. Structure 27, 1057–1070 e1054. [PubMed: 31155310]
19. Gottlieb L, and Marmorstein R (2018). Structure of Human NatA and Its Regulation by the Huntingtin Interacting Protein HYPK. Structure 26, 925–935 e928. [PubMed: 29754825]
20. Deng S, McTiernan N, Wei X, Arnesen T, and Marmorstein R (2020). Molecular basis for N-terminal acetylation by human NatE and its modulation by HYPK. Nature communications 11, 818.
21. Deng S, Pan B, Gottlieb L, Petersson EJ, and Marmorstein R (2020). Molecular basis for N-terminal alpha-synuclein acetylation by human NatB. eLife 9, e57491. [PubMed: 32885784]
22. Starheim KK, Kalvik TV, Bjørkøy G, and Arnesen T (2017). Depletion of the human N-terminal acetyltransferase hNaa30 disrupts Golgi integrity and ARFRP1 localization. Bioscience reports 37, BSR20170066.
23. Jumper J, Evans R, Pritzel A, Green T, Figurnov M, Ronneberger O, Tunyasuvunakool K, Bates R, Zidek A, Potapenko A, et al. (2021). Highly accurate protein structure prediction with AlphaFold. Nature 596, 583–589. [PubMed: 34265844]
24. Dephoure N, Zhou C, Villen J, Beausoleil SA, Bakalarski CE, Elledge SJ, and Gygi SP (2008). A quantitative atlas of mitotic phosphorylation. Proc Natl Acad Sci U S A 105, 10762–10767. [PubMed: 18669648]
25. Séraphin B (1995). Sm and Sm-like proteins belong to a large family: identification of proteins of the U6 as well as the U1, U2, U4 and U5 snRNPs. The EMBO journal 14, 2089–2098. [PubMed: 7744014]
26. Khusial P, Plaag R, and Zieve GW (2005). LSm proteins form heptameric rings that bind to RNA via repeating motifs. Trends Biochem.Sci 30, 522–528. [PubMed: 16051491]
27. Knorr AG, Schmidt C, Tesina P, Berninghausen O, Becker T, Beatrix B, and Beckmann R (2019). Ribosome-NatA architecture reveals that rRNA expansion segments coordinate N-terminal acetylation. Nat Struct Mol Biol 26, 35–39. [PubMed: 30559462]
28. Koufaris C, and Kirmizis A (2020). N-Terminal Acetyltransferases Are Cancer-Essential Genes Prevalently Upregulated in Tumours. Cancers 12, 2631. [PubMed: 32942614]
29. Evjenth R, Hole K, Karlsen OA, Ziegler M, Arnesen T, and Lillehaug JR (2009). Human Naa50p (Nat5/San) displays both protein N alpha- and N epsilon-acetyltransferase activity. J Biol Chem 284, 31122–31129. [PubMed: 19744929]

30. Tercero JC, Dinman JD, and Wickner RB (1993). Yeast MAK3 N-acetyltransferase recognizes the N-terminal four amino acids of the major coat protein (gag) of the L-A double-stranded RNA virus. J Bacteriol 175, 3192–3194. [PubMed: 8491733]

31. Wu T, Yu J, Gale-Day Z, Woo A, Suresh A, Hornsby M, and Gestwicki JE (2020). Three Essential Resources to Improve Differential Scanning Fluorimetry (DSF) Experiments. bioRxiv, 2020.2003.2022.002543.

32. Zheng SQ, Palovcak E, Armache JP, Verba KA, Cheng Y, and Agard DA (2017). MotionCor2: anisotropic correction of beam-induced motion for improved cryo-electron microscopy. Nature methods 14, 331–332. [PubMed: 28250466]

33. Zivanov J, Nakane T, Forsberg BO, Kimanius D, Hagen WJH, Lindahl E, and Scheres SHW (2018). New tools for automated high-resolution cryo-EM structure determination in RELION-3. eLife 7, e42166. [PubMed: 30412051]

34. Rohou A, and Grigorieff N (2015). CTFFIND4: Fast and accurate defocus estimation from electron micrographs. Journal of structural biology 192, 216–221. [PubMed: 26278980]

35. Punjani A, Rubinstein JL, Fleet DJ, and Brubaker MA (2017). cryoSPARC: algorithms for rapid unsupervised cryo-EM structure determination. Nature methods 14, 290–296. [PubMed: 28165473]

36. Emsley P, and Cowtan K (2004). Coot: model-building tools for molecular graphics. Acta Crystallogr D Biol Crystallogr 60, 2126–2132. [PubMed: 15572765]

37. Jones DT (1999). Protein secondary structure prediction based on position-specific scoring matrices. J Mol Biol 292, 195–202. [PubMed: 10493868]

38. Adams PD, Afonine PV, Bunkoczi G, Chen VB, Davis IW, Echols N, Headd JJ, Hung LW, Kapral GJ, Grosse-Kunstleve RW, et al. (2010). PHENIX: a comprehensive Python-based system for macromolecular structure solution. Acta Crystallogr D Biol Crystallogr 66, 213–221. [PubMed: 20124702]

39. Pettersen EF, Goddard TD, Huang CC, Couch GS, Greenblatt DM, Meng EC, and Ferrin TE (2004). UCSF Chimera--a visualization system for exploratory research and analysis. J Comput Chem 25, 1605–1612. [PubMed: 15264254]

40. Schrodinger LLC (2015). The PyMOL Molecular Graphics System, Version 1.8

41. Zivanov J, Nakane T, Forsberg BO, Kimanius D, Hagen WJ, Lindahl E, and Scheres SH (2018). New tools for automated high-resolution cryo-EM structure determination in RELION-3. Elife 7, e42166. [PubMed: 30412051]

42. Sievers F, Wilm A, Dineen D, Gibson TJ, Karplus K, Li W, Lopez R, McWilliam H, Remmert M, Söding J, et al. (2011). Fast, scalable generation of high-quality protein multiple sequence alignments using Clustal Omega. Molecular Systems Biology 7, 539. [PubMed: 21988835]

43. Robert X, and Gouet P (2014). Deciphering key features in protein structures with the new ENDscript server. Nucleic Acids Res 42, W320–324. [PubMed: 24753421]

Highlights

- Naa38 broadens the substrate-specificity profile of NatC
- Naa38 reorients an NAA30 N-terminal peptide binding loop for optimal catalysis
- Naa38 orders an N-terminal segment of NAA35 and increases NatC thermostability
- Unlike in yeast, Inositol hexaphosphate (IP_6) does not contribute to NatC stability

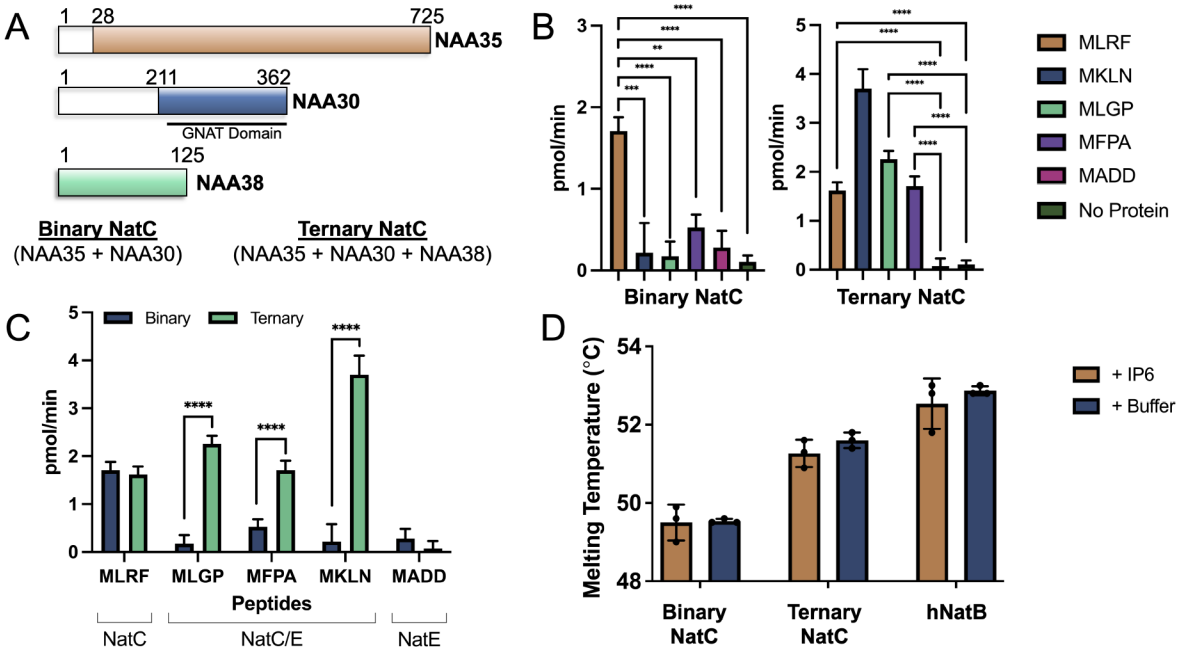

Figure 1. Contributions of hNAA38 to hNatC catalytic activity and thermostability.

(A) Schematic representation of protein constructs (color-filled regions) that were used to prepare recombinant hNatC complexes. The “binary NatC” complex contains hNAA35 and hNAA30, while the “ternary NatC” complex also contains hNAA38. The GNAT domain of hNAA30 consists of residues 211–362. **(B)** Acetylation activity (pmol/min acetylated product) of binary and ternary hNatC complexes against an MLRF NatC cognate peptide, MLGP, MKLN, MFPA NatC/E cognate peptide substrate, and MADD NatE cognate peptide substrate., (**P ≤ 0.01,*** P ≤ 0.001, **** P ≤ 0.0001, not significant (ns) not shown). Acetylation rates were calculated from independent replicates, therefore no individual points are shown. Error bars indicate the SEM for each reported point, (Binary peptide MLRF, MLGP and MKLN are in duplicate, and all others in triplicate). **(C)** Comparison of acetylation activity between binary (tan) and ternary (purple) NatC (**** P≤0.0001, ns not shown). Error bars indicate the SEM for each reported point, (Binary peptide MLRF, MLGP and MKLN are in duplicate, all others in triplicate). **(D)** Differential scanning fluorimetry (DSF) evaluation of both the binary and ternary hNatC complexes and the hNatB complex performed with (blue) circle or without IP_6 (purple). Average calculated melting temperature transitions are indicated as the middle line. Error bars in Panel C indicate the SD for each reported melting temperature, n = 3 (technical replicates).

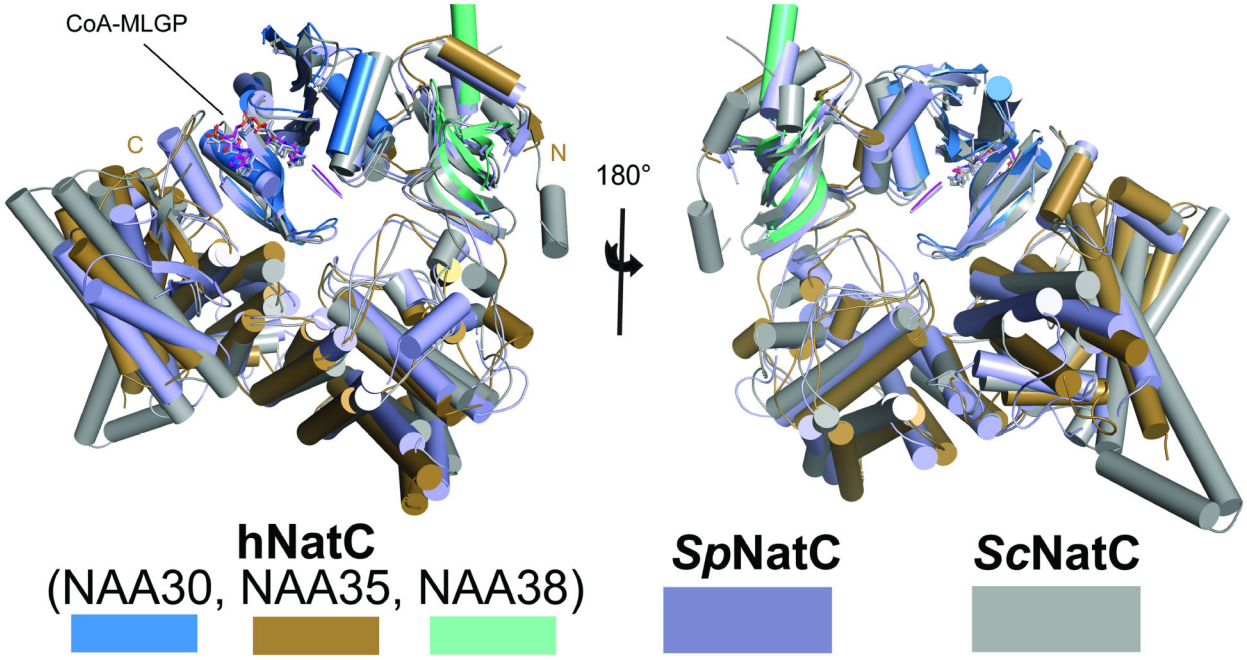

Figure 2. The overall architecture of the ternary hNatC complex and comparison with yeast NatC complexes.

hNatC structure colored by subunits (hNAA30, blue; hNAA35, brown; hNAA38, Cyan) is shown in cartoon and aligned with *Sp*NatC (light blue) and *Sc*NatC (grey). For reference, the N- and C-terminal ends of hNAA35 and the CoA-MLGP inhibitor are labeled.

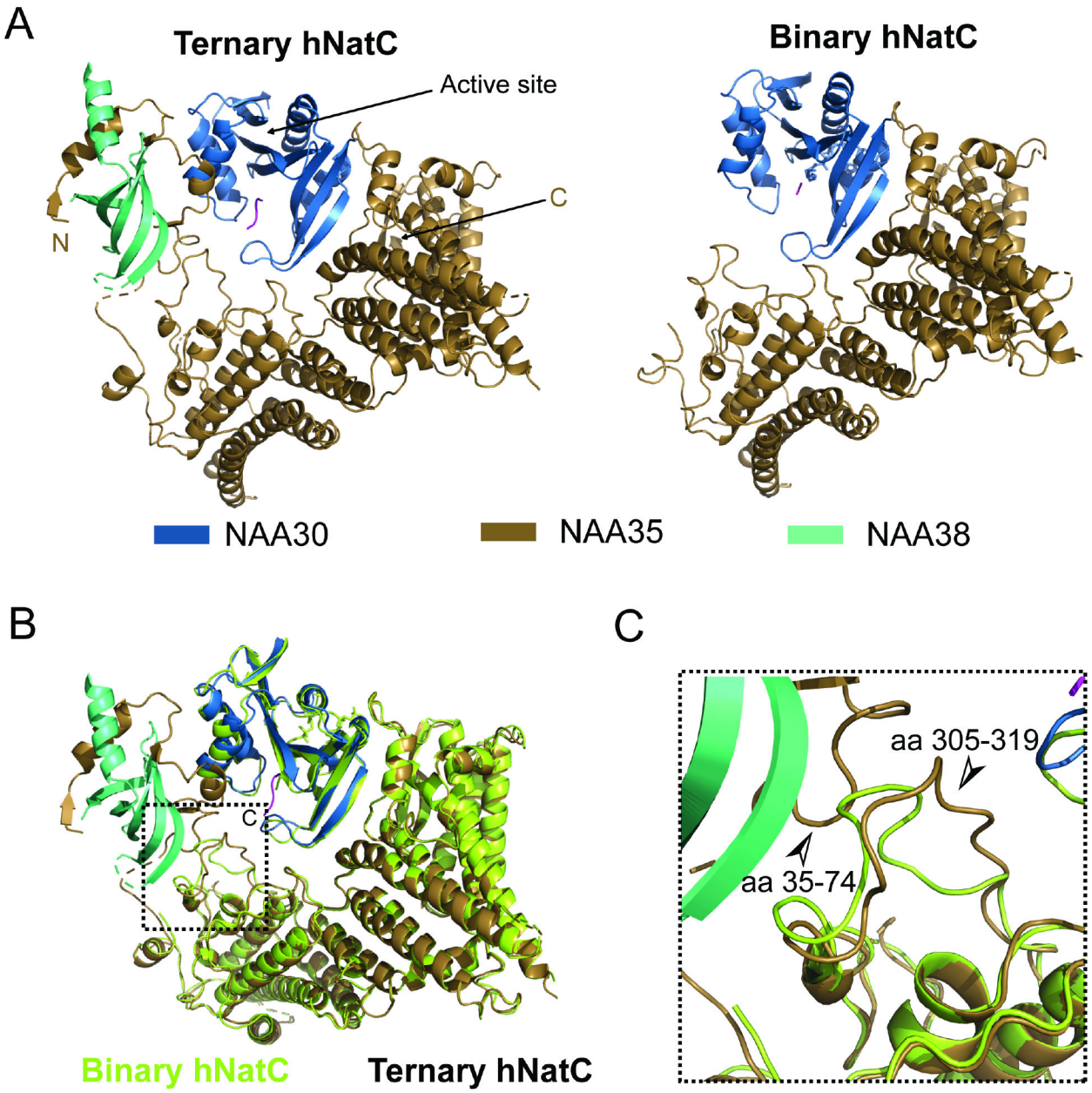

Figure 3. Comparison of the ternary and binary hNatC structures.

(A) Binary and ternary hNatC complexes are shown in cartoon and side-by-side, with hNAA30 (blue), hNAA35 (brown), hNAA38 (green). For reference, the N- and C-terminal ends of hNAA35 and the active site are labeled. **(B)** Ternary hNatC (colored as in panel A) is overlayed with binary hNatC (lime) with a dashed box surrounding the region that is magnified in panel C. **(C)** Zoomed-in view highlighting the rearrangement of hNAA35 loops containing residues 35–74 and 305–319 (arrows), hNAA38 β-sheets arising from hNAA38 binding in the ternary hNatC complex.

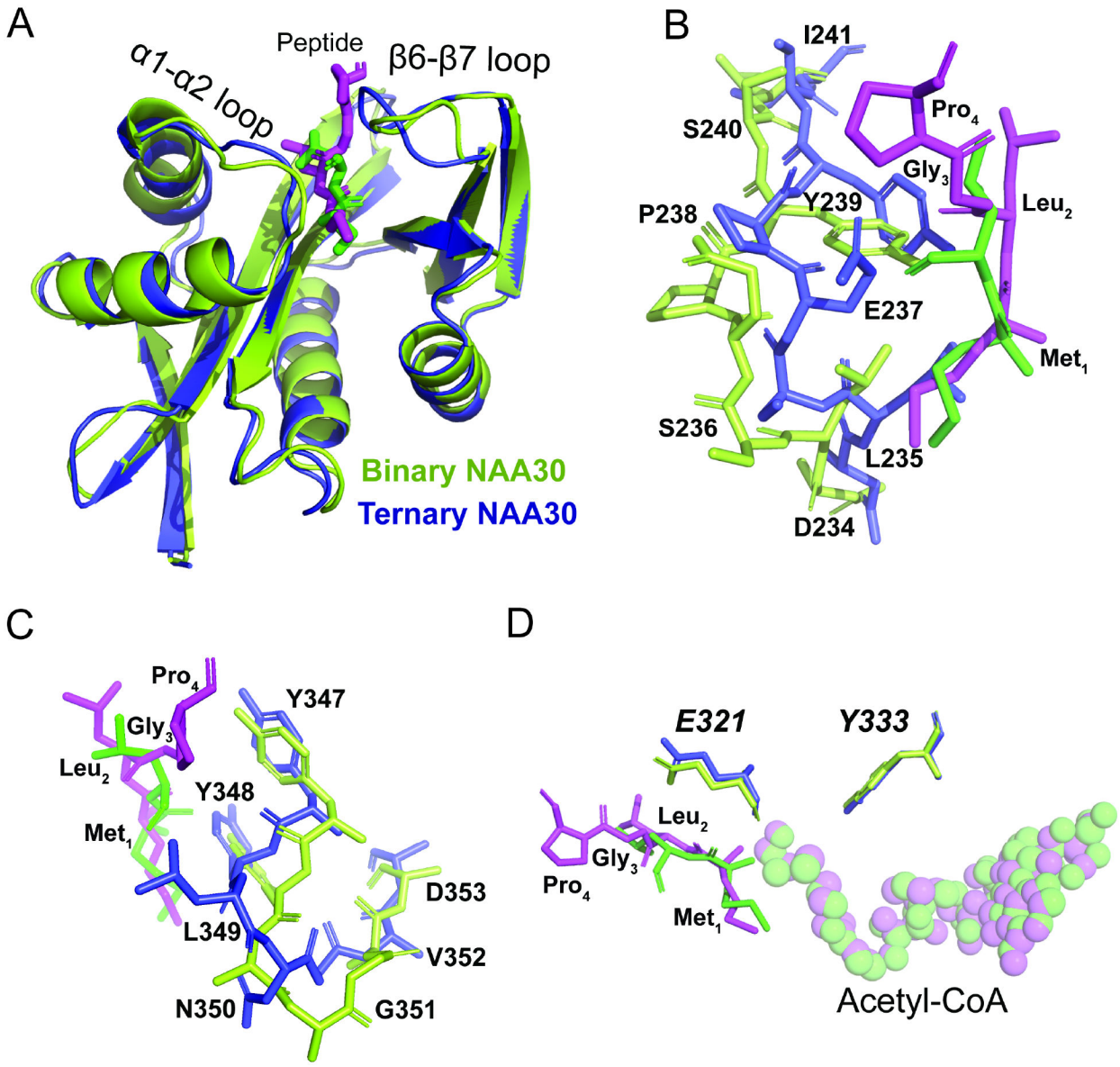

Figure 4. Comparison of peptide substrate binding in the ternary and binary hNatC structures.

(A) Superposition of binary and ternary hNAA30 (lime and blue, respectively) are shown as cartoon. Resolved portions of the peptide substrates of the binary and ternary hNatC complexes are shown in green and magenta sticks, respectively. Residues from **(B)** hNAA30 α1-α2 loop and **(C)** hNAA30 β6-β7 loop in the ternary hNatC (blue sticks) that interact with the peptide substrate portion are highlighted and superimposed with the corresponding, binary hNatC residues (lime sticks). **D)** Superposition of catalytic residues hNAA30-E321 and Y333 in the binary and ternary structures. Acetyl-CoA is shown as a CPK model.

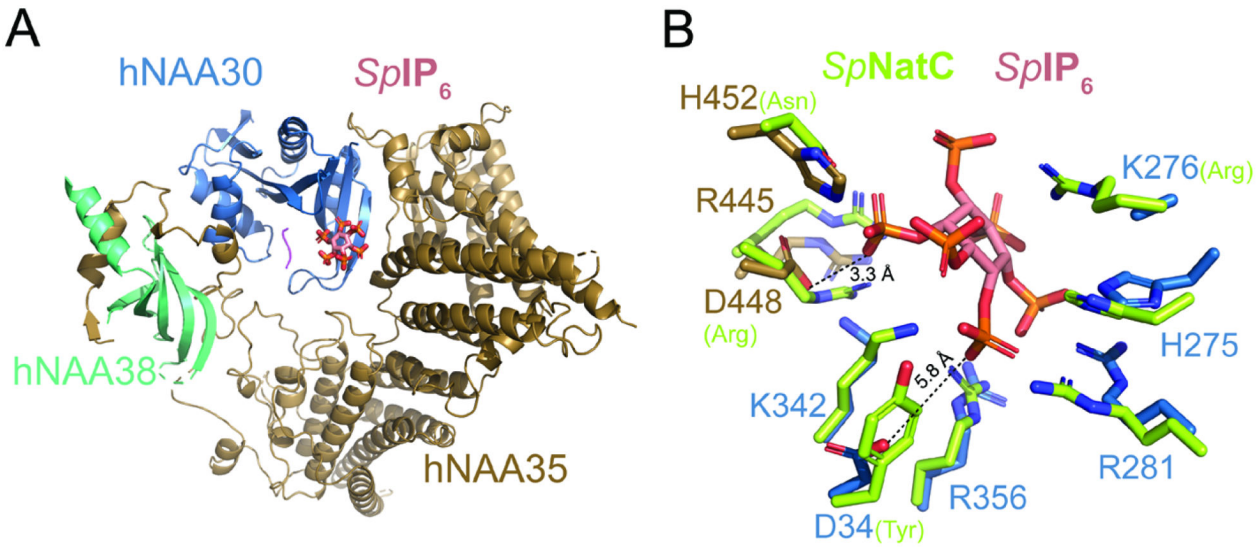

Figure 5. Suboptimal IP_6 binding properties of hNatC.

(A) IP_6 (*Sp*IP_6, orange sticks) from *Sp*NatC (PDB: 7L1K) is superimposed onto the ternary hNatC structure. **(B)** Residues mediating interactions with *Sp*IP_6 in *Sp*NatC structure are colored in green and superimposed with overlapping residues from hNAA30 (blue) and hNAA35 (brown). K276 of hNAA30 is disordered and modeled as an alanine. The distance between the D341 side chain of hNAA30 and *Sp*IP_6 is ~3.3 Å, while the distance between the D448 side chain of hNAA35 and *Sp*IP_6 is ~5.8 Å.

KEY RESOURCES TABLE

REAGENT or RESOURCE	SOURCE	IDENTIFIER
Bacterial and Virus Strains		
Spodoptera frugiperda (Sf9) cells	Invitrogen	Cat#11496015
E. coli Rosetta (DE3)pLysS	EMD Millipore	Cat#70956-3
ScarabXpress T7lac	(Scarab Genomics)	Cat#C-1709-05K
Chemicals, Peptides, and Recombinant Proteins		
GST-NAA38$^{1-125}$	This Paper	N/A
Binary hNatC (hNAA30$^{211-362}$ /hNAA35$^{28-725}$)	This Paper	N/A
Ternary hNatC (hNAA30$^{211-362}$ /hNAA35$^{28-725}$/hNAA38$^{1-125}$)	This Paper	N/A
hNatB (hNAA25$^{1-972}$/hNAA20$^{1-163}$)	[21]	N/A
Nickel Resin	Thermo Scientific	Cat#88223
HiTrap SP HP, 5 mL	GE Healthcare	Cat#17115201
Superdex 200 10/300 GL	GE Healthcare	Cat#17517501
[14C]Acetyl-CoA (4 mCi/mmol)	PerkinElmer Life Sciences	Cat#NEC313050UC
P81 Phosphocellulose squares	St. Vincent's Institute Medical Research	N/A
CoA-Ac-MLGPE-NH2 bisubstrate inhibitor	[18]	N/A
MLGP Peptide (NH_2-MLGPEGGRWGRPVGRRRRP-COOH)	Genscript	N/A
MKLN Peptide (NH_2-MKLNISFRWGRPVGRRRRP-COOH)	Genscript	N/A
MFPA peptide (NH_2-MFPAAPSRWGRPVGRRRRP-COOH)	Genscript	N/A
MADD peptide (NH_2-MADDLDFRWGRPVGRRRRP-COOH)	Genscript	N/A
MLRF peptide (NH_2-MLRFVTKRWGRPVGRRRRP-COOH)	Genscript	N/A
Deposited Data		
Atomic coordinates for binary hNatC	This paper	PDB-7RB3
Atomic coordinates for ternary hNatC	This paper	PDB-7MX2
Atomic coordinates for ternary *Sp*NatC	[17]	PDB-71LK
Atomic coordinates for ternary *Sc*NatC	[10]	PDB-6YGB
Cryo-EM map for binary hNatC	This paper	EMD-24393
Cryo-EM map for ternary hNatC	This paper	EMD-24070
Recombinant DNA		
pRSF vector GST-TEV-hNAA38$^{1-125}$	This paper	N/A
pFASTBacDUAL His_6-TEV-hNAA35$^{28-725}$ + hNAA30$^{211-362}$	This paper	N/A
Primers for recombinant NatC: Supplementary Table 1	This paper	N/A
Software and Algorithms		
Phenix	[38]	https://www.phenix-online.org/documentation/reference/refinement.html
RELION	[41]	N/A
MotionCor2	[32]	N/A

REAGENT or RESOURCE	SOURCE	IDENTIFIER
CryoSPARC	35	N/A
COOT	36	https://www2.mrc-lmb.cam.ac.uk/personal/pemsley/coot/
PyMOL	Schrodinger LLC	http://www.pymol.org
Prism 9.0	GraphPad	https://www.graphpad.com/scientific-software/prism/
Clustal Omega	42	https://www.ebi.ac.uk/Tools/msa/clustalo/
ESPript 3.0	43	http://espript.ibcp.fr/ESPript/ESPript/

Table 1 |

Cryo-EM data collection, refinement and validation statistics

	Ternary hNatC EMD-24070, PDB-7MX2	**Binary hNatC EMD-24393, PDB-7RB3**
Data collection and processing		
Magnification	105,000	105,000
Voltage (keV)	300	300
Electron exposure (e/Å^2)	42	42
Defocus range (μm)	−1.0 to −3.0	−1.0 to −3.0
Pixel size (Å)	0.42	0.42
Number of images	5,372	4,222
Symmetry imposed	C1	C1
Initial particles (no.)	1,606,636	2,539,386
Final particles (no.)	172,041	192,437
Map resolution (Å)	3.64	3.09
FSC threshold	0.143	0.143
Refinement		
Initial model used (PDB code)	7L1K	7MX2
Model resolution (Å)	3.8	3.4
FSC threshold	0.5	0.5
Map sharpening *B* factor (Å^2)	−213.6	−135.6
Model composition		
Non-hydrogen atoms	6762	5973
Protein residues	875	750
Ligands	1	1
***B* factors (Å^2)**		
Protein	22.48/135.72/71.95	14.23/134.90/57.99
Ligand	90.36/90.36/90.36	65.39/65.39/65.39
R.M.S. deviations		
Bonds lengths (Å)	0.003	0.004
Bond angles (°)	0.582	0.639
Validation		
MolProbity score	1.48	1.57
Clash score	4.10	5.33
Poor rotamers (%)	0.00	0.26
Ramachandran plot		
Favored (%)	95.91	96.12
Allowed (%)	4.09	3.88
Disallowed (%)	0.00	0.00